Inorganic Chemistry

Article

pubs.acs.org/IC

Nanostructured SnO_2–ZnO Heterojunction Photocatalysts Showing Enhanced Photocatalytic Activity for the Degradation of Organic Dyes

Md. Tamez Uddin,[†] Yohann Nicolas,[†] Céline Olivier,[†] Thierry Toupance,*[,†] Laurent Servant,[†] Mathis M. Müller,[‡] Hans-Joachim Kleebe,[‡] Jürgen Ziegler,[‡] and Wolfram Jaegermann[‡]

[†]University of Bordeaux, Institut des Sciences Moléculaires, UMR 5255 CNRS, 351 Cours de la Libération, F-33405 Talence Cedex, France

[‡]Institute of Material Science, Technische Universität Darmstadt, Petersenstrasse 23, D-64287 Darmstadt, Germany

Supporting Information

ABSTRACT: Nanoporous SnO_2–ZnO heterojunction nanocatalyst was prepared by a straightforward two-step procedure involving, first, the synthesis of nanosized SnO_2 particles by homogeneous precipitation combined with a hydrothermal treatment and, second, the reaction of the as-prepared SnO_2 particles with zinc acetate followed by calcination at 500 °C. The resulting nanocatalysts were characterized by X-ray diffraction (XRD), FTIR, Raman, X-ray photoelectron spectroscopy (XPS), nitrogen adsorption–desorption analyses, transmission electron microscopy (TEM), and UV–vis diffuse reflectance spectroscopy. The SnO_2–ZnO photocatalyst was made of a mesoporous network of aggregated wurtzite ZnO and cassiterite SnO_2 nanocrystallites, the size of which was estimated to be 27 and 4.5 nm, respectively, after calcination. According to UV–visible diffuse reflectance spectroscopy, the evident energy band gap value of the SnO_2–ZnO photocatalyst was estimated to be 3.23 eV to be compared with those of pure SnO_2, that is, 3.7 eV, and ZnO, that is, 3.2 eV, analogues. The energy band diagram of the SnO_2–ZnO heterostructure was directly determined by combining XPS and the energy band gap values. The valence band and conduction band offsets were calculated to be 0.70 ± 0.05 eV and 0.20 ± 0.05 eV, respectively, which revealed a type-II band alignment. Moreover, the heterostructure SnO_2–ZnO photocatalyst showed much higher photocatalytic activities for the degradation of methylene blue than those of individual SnO_2 and ZnO nanomaterials. This behavior was rationalized in terms of better charge separation and the suppression of charge recombination in the SnO_2–ZnO photocatalyst because of the energy difference between the conduction band edges of SnO_2 and ZnO as evidenced by the band alignment determination. Finally, this mesoporous SnO_2–ZnO heterojunction nanocatalyst was stable and could be easily recycled several times opening new avenues for potential industrial applications.

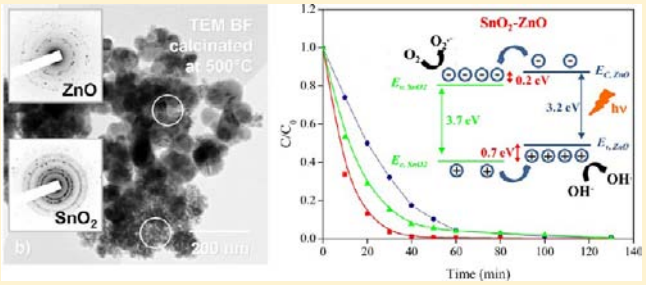

1. INTRODUCTION

Over the past two decades, the preparation of nanostructured nanoporous metal oxide semiconductors has been the subject of intense research efforts because of their unique chemical, electronic, and optical properties and their numerous potential or demonstrated applications. Thus, nanostructured semiconductor metal oxide photocatalysts, as titanium dioxide (TiO_2) or zinc oxide (ZnO) nanoparticles, have been proposed as an alternative to the conventional methods (i.e., adsorption, biological degradation, chlorination, or ozonation processes) for the complete removal of toxic chemicals from the industrial hazards.[1] In this case, the creation of electron–hole pairs upon UV-irradiation promotes the formation of powerful oxidizing agents on the surface of metal oxide nanocrystals that favors the decomposition of organic compounds and pollutants.[2] Nonetheless, this approach still suffers from some limitations because of the fast recombination of the photogenerated electron–hole pairs hampering industrial application of photocatalytic techniques in the degradation of contaminants in water and air.[3] As a consequence, minimizing the recombination of photogenerated electron–hole pairs before their participation in redox processes constitutes a key issue for enhancing the photocatalytic efficiency of such materials. To draw a new prospect in this field, heterostructure photocatalysts combining two metal oxide semiconductors of different electron affinity and ionization potentials were developed using contact or core–shell type morphologies (Scheme 1). When such a heterostructure is irradiated with UV-light, valence band (VB) electrons are excited to the conduction band (CB) with simultaneous generation of the same amount of holes in the VB. Photogenerated electrons are then injected from the CB of the semiconductor with an energetically higher CB edge to the CB of the semiconductor with lower CB edge. Simultaneously, holes are injected in the opposite direction for appropriate VB offsets, thus

Received: April 17, 2012
Published: June 26, 2012

   dx.doi.org/10.1021/ic300794j | Inorg. Chem. 2012, 51, 7764–7773

Scheme 1. Schematic Representation of the Charge Separation Processes for the Heterostructure Photocatalysts in Contact Type (*left*) and Core-Shell Type (*right*) Geometries

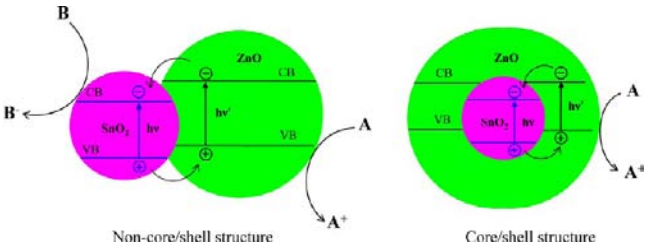

increasing the rate of charge separation and reducing the electron−hole pair recombination. In both contact type and core/shell type semiconductors, the charge separation mechanism is the same. However, both holes and electrons are accessible for selective oxidation and reduction processes on different particle surfaces in contact type semiconductor heterostructures, while only one charge carrier is accessible in the core−shell type analogue leading to selective charge transfer at the semiconductor electrolyte interface.[4] In this context, various semiconductor-based heterostructure photocatalysts have been designed and investigated such as TiO_2−ZnO,[5] TiO_2−WO_3,[6] and ZnO-WO_3.[7] Among the binary metal oxides, tetragonal tin dioxide, SnO_2, is a well-known large band gap multifunctional material that found widespread applications in the fields of Li-batteries,[8] field emission,[9] gas sensing,[10] and photovoltaic conversion.[11] Because of its more positive CB edge, SnO_2 is a better electron acceptor than TiO_2 and ZnO that makes it a good candidate for the above-mentioned heterostructures. As a consequence, associating SnO_2 with ZnO has been the subject of several reports for achieving an efficient charge separation and improving the photocatalytic properties of both oxides. In this context, various strategies have been investigated to produce ZnO-SnO_2 heterostructures including co-precipitation method followed by calcination,[12] hydrothermal or solvothermal routes,[13] and sol−gel process combined with electrospinning techniques.[14] ZnO-SnO_2 heterostructures with a molar ratio Zn:Sn of 2:1 prepared by the co-precipitation method showed higher photocatalytic decomposition rates of methyl orange (MO) than pure ZnO and SnO_2 analogues.[12a,f] A similar trend has been also described by Zhang et al. for one-dimensional ZnO-SnO_2 nanofibers synthesized by an electrospinning technique.[14] However, even though it has been reported that the enhanced photocatalytic properties found with ZnO-SnO_2 heterostructures were related to improved charge separation, no determination of the band alignment in such system has been reported so far to confirm this feature. Thus, the photocatalytic activity of ZnO-SnO_2 systems still remains largely unexplored. On the other hand, one-pot synthesis combined with annealing at high temperature can lead to crystalline impurities as Zn_2SnO_4[12a−e] which requires the development of alternative preparation procedures.

As a consequence, we herein report on the characterization and the photocatalytic properties of SnO_2−ZnO materials prepared by a simple two-step procedure. Nanosized SnO_2 particles were first prepared by homogeneous precipitation coupled with hydrothermal treatment and, then, reacted with zinc acetate in acidic medium followed by calcination in air to grow ZnO particles. The photocatalytic activity and recycling ability of the resulting SnO_2−ZnO heterostructure were investigated by the degradation of methylene blue (MB) dye under UV irradiation and compared to those of SnO_2 and ZnO nanopowders. To gain a deeper insight in the relationship between the electronic properties and the photocatalytic activity, the band alignment of the SnO_2−ZnO photocatalyst was carefully determined by UV−visible diffuse reflectance and X-ray Photoelectron spectroscopies. The enhanced photocatalytic properties of the SnO_2−ZnO photocatalysts were rationalized in terms of a better charge separation related to the effective semiconductor heterojunction.

2. EXPERIMENTAL SECTION

2.1. Preparation of Nanosized Metal Oxide Photocatalysts. Anhydrous tin tetrachloride (Acros Organic), zinc acetate dihydrate (Alfa Aesar), sodium bicarbonate (Alfa Aesar), and urea (Sigma Aldrich) of analytical grade were used without further purification. Nanocrystalline SnO_2 colloids were first prepared by homogeneous precipitation using a procedure adapted from literature.[15] In a typical experiment, 2.08 g (0.04 M) of anhydrous $SnCl_4$ and 14.4 g (1.2 M) of urea, used as the precipitant, were mixed in 200 mL of deionized water. The solution was then heated at 90 °C for 4 h. The resulting precipitates were filtered and washed with distilled water. The solids obtained were then dispersed in 100 mL aqueous solution of acetic acid (pH 2) and subjected to hydrothermal treatment in an autoclave at 240 °C for 16 h. The resulting suspension was then condensed to a final SnO_2 concentration of 10−15 wt % by a rotary evaporator. The latter suspension was then divided into two parts. The first one was dried at 90 °C overnight and then calcined in air at 500 °C for 90 min. To prepare the SnO_2−ZnO heterostructure with a 1:1 molar ratio, 0.437 g of $Zn(CH_3COO)_2{\cdot}2H_2O$ was added to 5 g of the 12 wt % SnO_2 aqueous suspension. After stirring for 12 h, the resulting mixture was dried at 90 °C overnight and then annealed in air at 500 °C for 2 h to yield the hereafter named SnO_2−ZnO photocatalyst. Finally, ZnO was prepared by precipitation method:[16] to a solution of 5.5 g of $Zn(CH_3COO)_2{\cdot}2H_2O$ in distilled water (100 mL), and under continuous stirring, was added an aqueous solution of sodium bicarbonate until reaching a neutral pH. After filtration of the precipitate, the latter was dried at 110 °C overnight and subsequently calcined at 500 °C in air for 2 h to give the herafter named ZnO photocatalyst. The different powders prepared were crushed with pestle and mortar before further characterization and photocatalytic experiments.

2.2. Characterization. Fourier Transform Infrared (FTIR) studies (KBr pellets) were performed with a Perkin-Elmer spectrum 100 FTIR spectrophotometer. Raman spectra were recorded in the solid state on a Labram 1B spectrometer using a red laser beam (632 nm). X-ray diffraction (XRD) studies were carried out with a Bruker AXS diffractometer (D2 PHASER A26-X1-A2B0D3A) using a Cu anode (Kα radiation). A continuous scan mode was used to collect 2θ data from 10 to 80° with a 0.1° sampling pitch and a 2° min^{-1} scan rate. The average crystallite size of the materials prepared was estimated by fwhm (full width at half-maximum) according to Scherrer's formula (applied to the {110} reflection), $D = (0.9\,\lambda)/(\beta_{1/2}\cos\theta_B)$, where D is the average grain size, λ is the wavelength of Cu K_α (= 1.5405 Å), $\beta_{1/2}$ is the fwhm, and θ_B is the diffraction angle. Transmission electron microscopy was performed using a Jeol JEM 2100F (Jeol, Tokyo, Japan) operating at an acceleration voltage of 200 kV (wavelength λ = 2.51 pm) equipped with a Schottky-type FEG and an EDS system (Oxford, Wiesbaden, Germany). For transmission electron microscopy (TEM) sample preparation, the photocatalysts were dispersed in an ultrasonic bath (high purity methanol 99.8%, Sigma−Aldrich Co.) and a small droplet of the suspension was placed on holey carbon (Cu) grid. Upon drying, the samples were lightly coated with carbon to avoid charging under the electron beam. Nitrogen sorption isotherms (77 K) were recorded with an Micromeritics ASAP2010 equipment. Before each analysis, samples were degassed at 120 °C in vacuum for a time interval long enough to reach a constant pressure (<10 μm Hg). The specific surface areas (S_{BET}) were calculated using the Brunauer−Emmett−Teller (BET) equation between 0.1 and 0.3 relative pressure (P/P_0). Mesopore size distributions were deduced from the Barrett, Joyner, Halenda (BJH) method applied to the adsorption branch of the nitrogen adsorption isotherm.[17] The calculation was performed by the Micromeritics software package which uses the recurrent method and applies the Harkins and Jura equation for the

dx.doi.org/10.1021/ic300794j | Inorg. Chem. 2012, 51, 7764−7773

multilayer thickness. UV−vis diffuse reflectance spectra were measured at room temperature in the 200−800 nm wavelength range using an UV−vis-NIR spectrometer (Lambda 900). Pure powdered $BaSO_4$ was used as a reference sample. X-ray Photoelectron spectra were recorded using a PHOIBOS 225 (Specs GmbH) spectrometer. Monochromatized X-ray (K_α: 1486.61 eV) from an Al anode was used for excitation. The charge effect was evaluated using the main component of the C 1s peak, associated with adventitious hydrocarbons with a binding energy of 284.8 eV as reference for calibration. The base pressure in the sample during the measurements was less than 3×10^{-8} mbar. The energy band diagram of the SnO_2−ZnO heterostructure was determined by X-ray photoelectron spectroscopy (XPS) using well-known procedures from the literature.[18] The technique consists of first measuring the Sn 3d and Zn 2p core levels as well as the VB maximum (VBM) E_V of the bulk SnO_2 and bulk ZnO, respectively. These values were measured by XPS acquisitions on each kind of film deposited by the drop-casting method onto Al substrate. The position of the Sn 3d and Zn 2p core levels of the SnO_2−ZnO heterostructure was then determined. These last values were obtained from XPS acquisitions on the film of SnO_2−ZnO heterostructure deposited on Al substrate. The VB offset (VBO) ΔE_V of the heterostructure SnO_2/ZnO was then calculated according to eq 1[19]

$$\Delta E_V = (E_{Zn\cdot 2p} - E_{V\cdot ZnO})^{ZnO}_{bulk} - (E_{Sn\cdot 3d} - E_{V\cdot SnO_2})^{SnO_2}_{bulk} - \Delta E_{CL} \quad (1)$$

where $\Delta E_{CL} = (E_{Zn\cdot 2p} - E_{Sn\cdot 3d})_{heterostructure}$ is the energy difference between Zn 2p and Sn 3d core levels (CLs), which were measured in the SnO_2−ZnO sample. $E_{Zn\cdot 2p}$ and $E_{Sn\cdot 3d}$ are the binding energies in the bulk of ZnO and SnO_2, respectively; $E_{V.ZnO}$ and $E_{V\cdot SnO_2}$ are the VB maxima in the bulk of ZnO and SnO_2, respectively.

2.3. Photocatalytic Experiments. Photocatalytic activities of the as-synthesized samples were evaluated by the degradation of MB (Alfa Aesar) dye. The MB was reagent grade and was used as supplied. All the experiments were conducted at room temperature in air. In each experiment, 0.1 g of metal oxide catalyst was dispersed in 100 mL of MB solution (10 mg/L) to obtain the concentration of the catalyst at 1.0 g/L. The experiments were carried out in a Pyrex beaker illuminated with a 125 W high pressure mercury lamp (Philips, HPL-N 125 W/542 E27) emitting UV light (365 and 313 nm). The UV lamp was positioned above the beaker containing the solution. Prior to irradiation, the suspension was stirred in the dark for 30 min to reach adsorption/desorption equilibrium. The solution was continuously stirred during the experiments. At given irradiation time intervals, 4 mL of the suspension were collected, and then centrifuged (4000 rpm, 10 min) to separate the photocatalyst particles. The MB concentration was evaluated by UV−visible Spectrophotometer (Shimadzu, UV-1650 pc) monitoring the absorption maximum at λ_{max} = 664 nm. A calibration plot based on Beer−Lambert's law was established by relating the absorbance to the concentration. In each case, blank experiments were also conducted with the catalysts in the absence of light and without the catalysts when the solution containing the dissolved dye was illuminated. Moreover, reference experiments were performed under the same conditions with commercial TiO_2 (Degussa, P-25) used as a photocatalytic standard. In some cases, repetitive photodegradation of MB during four consecutive cycles was performed with 1.0 g/L of catalyst at 10 mg/L dye concentration. After each cycle, the catalyst was washed with distilled water and a fresh solution of MB was added before each photocatalytic run.

3. RESULTS AND DISCUSSION

3.1. Particle Characterization. Precipitation of SnO_2 was observed when a clear solution of $SnCl_4$ and urea was reacted at 90 °C in aqueous medium. The pH of the solution increased gradually because of the progressive decomposition of urea into NH_3 and CO_2, leading to the nucleation and growth of uniformly nanosized particles.[20] After annealing in air at high temperature, FTIR studies revealed the complete elimination of the undesirable organics and the formation of metal oxide species (Figure 1A). Thus, above 2000 cm^{-1}, a very broad absorption around 3430 cm^{-1}

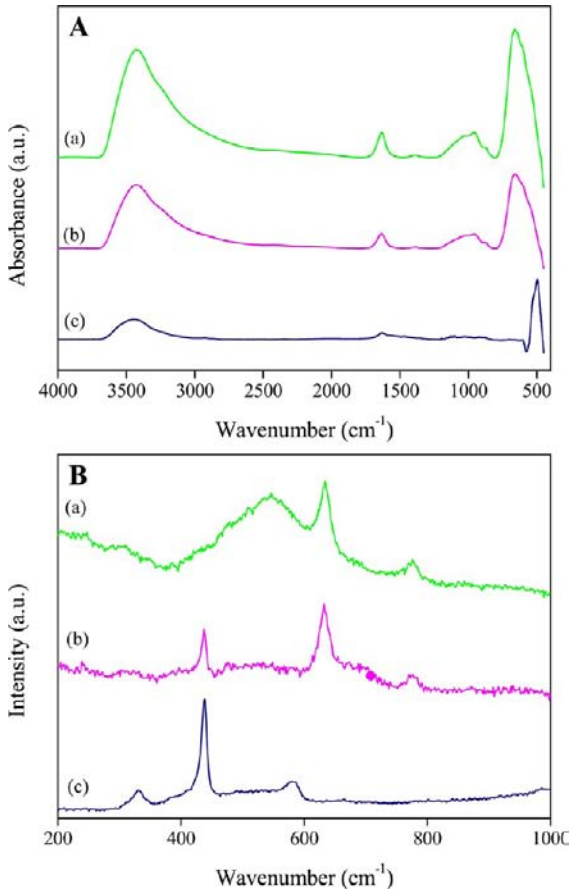

Figure 1. FTIR (**A**) and Raman (**B**) spectra of the as-synthesized photocatalysts after annealing in air at 500 °C; (a) SnO_2, (b) SnO_2−ZnO, and (c) ZnO.

ascribed to OH stretching vibration modes was observed for each sample.[21] Key features observed below 2000 cm^{-1} include a band at 1634 cm^{-1} due to the bending vibrations of absorbed molecular water, and wide bands at 659 cm^{-1} assigned to Sn−O stretching modes of Sn−O−Sn (Figures 1Aa-b)[22] and at 555 cm^{-1} due to Zn−O stretching modes (Figures 1Aa and 1Ac).[23] Furthermore, the Raman spectrum of the as-prepared SnO_2−ZnO photocatalyst showed three main features at 438, 632, and 776 cm^{-1} which could be assigned to the vibration modes E_2 for wurtzite ZnO[24] as well as A_{1g} and B_{2g} for cassiterite SnO_2.[25] Bands at 332 (second-order vibration originating from the zone boundary phonons)[26] and 585 (E_1(LO) mode) cm^{-1} were observed for the pure ZnO sample but were found to be very weak for the heterostructure. It is also worthwhile to mention that the broad resonance observed in the SnO_2 spectrum at 552 cm^{-1}, a feature that could be related to surface modes,[27] has collapsed after reaction with zinc acetate and further calcination. As a consequence, the signature of both wurtzite ZnO and cassiterite SnO_2 appeared in the Raman spectrum of the SnO_2−ZnO photocatalyst. This was confirmed by the XRD patterns of the materials calcined at 500 °C (Figure 2). All the diffraction lines in Figure 2a and 2c were those expected for the standard rutile-like, that is, cassiterite, crystalline structure of SnO_2 (space group: $P4_2/mmm$, JCPDS file no. 41-1445) and the standard hexagonal wurtzite ZnO (space group: $P6_3/mc$, JCPDS file no. 36-1451), respectively. The diffraction peaks of pure SnO_2 (Figure 2a) were considerably broadened revealing a small mean crystallite size which was estimated to be 5 ± 0.5 nm. On the other hand, the

dx.doi.org/10.1021/ic300794j | Inorg. Chem. 2012, 51, 7764−7773

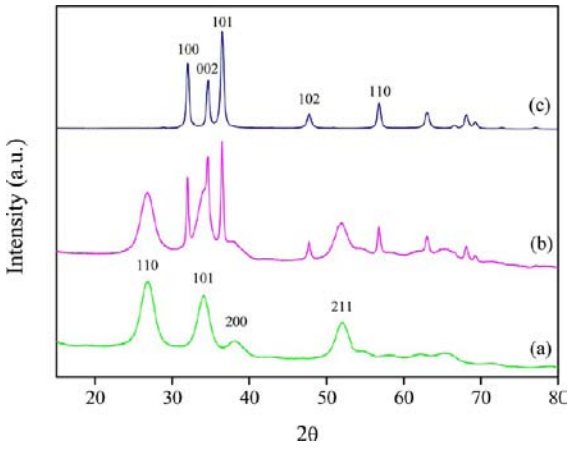

Figure 2. XRD patterns of the as-synthesized photocatalysts after annealing in air at 500 °C; (a) SnO_2, (b) SnO_2–ZnO, and (c) ZnO.

diffraction peaks of ZnO (Figure 2c) were rather sharp indicating a better crystallized sample, with an average crystallite size of about 18 ± 1 nm. ZnO seemed to calcine more easily and, thus, tends to have larger grain size than SnO_2. Furthermore, Figure 2b shows two sets of diffraction peaks for the SnO_2/ZnO sample ascribed to hexagonal wurtzite ZnO and cassiterite SnO_2. No additional peaks were observed in this sample that confirmed that the sample only contained nanocrystalline ZnO and SnO_2 particles. The full-width half-maximum (fwhm) for SnO_2 in SnO_2–ZnO photocatalyst is slightly larger than that found for pure SnO_2 showing that the size of the SnO_2 crystallite, that is, 4.5 ± 0.5 nm, in the SnO_2–ZnO photocatalyst was smaller than that in pure SnO_2. On the other hand, the crystallite size of ZnO, that is, 27 ± 1 nm, in SnO_2–ZnO was larger than that of pure ZnO. As previously reported for similar heterostructures,[12a] the presence of SnO_2 causes an increase in the crystallite size of ZnO whereas that of ZnO restrains the growth of SnO_2 nanocrystals.

Figure 3 shows TEM images of SnO_2–ZnO heterostructures dried at 90 °C (Figure 3a) and calcinated at 500 °C (Figure 3b). Moreover, HRTEM micrographs of the calcinated materials are shown to verify the crystallinity of both SnO_2 and ZnO after the heat treatment (Figures 3c,d). The shape of the pure SnO_2 nanoparticles was spherical and of uniform size (not shown here). It is worth mentioning that the diameter of the pure SnO_2 was about 5 nm which was in good agreement with the crystallite

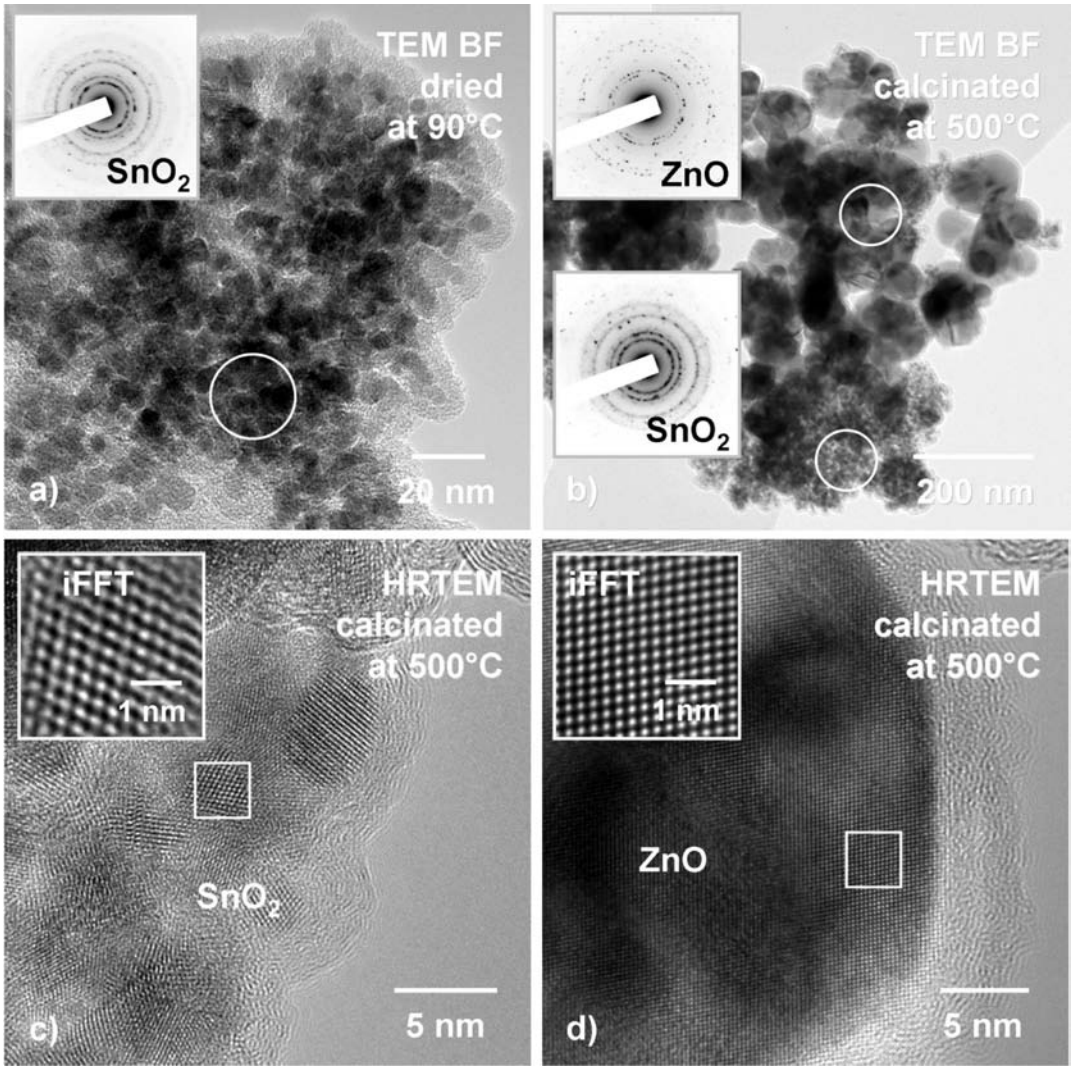

Figure 3. TEM micrographs of the (a) dried SnO_2–ZnO heterostructure and (b) calcinated SnO_2–ZnO photocatalyst. The inset SAED patterns reveal the occurrence of (a) crystalline SnO_2 and (b) crystalline SnO_2 and ZnO. HRTEM images (c,d) verify the crystallinity of both SnO_2 and ZnO after calcination.

dx.doi.org/10.1021/ic300794j | Inorg. Chem. 2012, 51, 7764–7773

size deduced from the XRD patterns. The dried SnO_2–ZnO heterostructure was composed of amorphous ZnO and nanocrystalline SnO_2, while upon hydrothermal treatment both phases were crystalline, as confirmed by the Selected Area Electron Diffraction (SAED) pattern shown in Figure 3b. According to the TEM bright field images, the SnO_2–ZnO photocatalyst was composed of aggregated ZnO particles of approximately 100 nm in diameter and nanosized SnO_2 particles, as also shown in the HRTEM images in Figures 3c and d. These results were consistent with those inferred from the above XRD analysis. Furthermore, a large number of small pores were observed between the nanoparticles suggesting that the SnO_2–ZnO photocatalyst is mesoporous. This feature was then assessed by N_2 sorption analyses. The N_2 adsorption–desorption isotherm of the SnO_2–ZnO heterostructure exhibited a type IV-like behavior including a type H2 hysteresis loop (Figure 4) which is typical of mesoporous

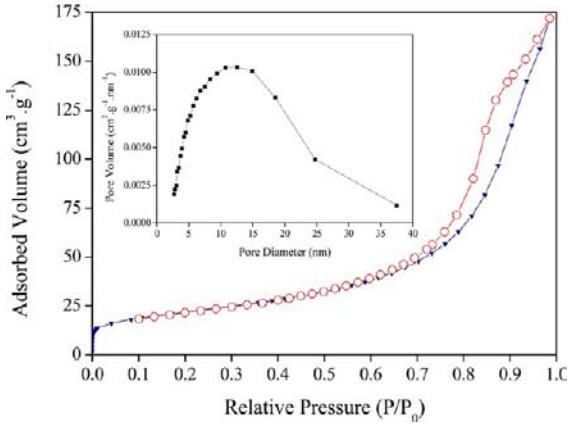

Figure 4. Nitrogen gas adsorption–desorption isotherms and pore-size distribution (inset) of the SnO_2–ZnO photocatalyst.

materials according to the IUPAC classification.[28] The H2-hysteresis loop indicated the presence of pores of nonuniform sizes and shapes, characteristic of solids consisting of particles crossed by nearly cylindrical channels or made by aggregates (consolidated) or agglomerates (unconsolidated) of spheroidal particles being fully consistent with the TEM data.[29] The BET surface area and pore volume for this system were estimated to be 77 ± 2 $m^2\ g^{-1}$ and 0.26 ± 0.01 $cm^3\ g^{-1}$, respectively; these values lay between those of pure SnO_2 and ZnO analogues (Table 1). Furthermore,

Table 1. Nitrogen Sorption Porosimetry Studies[a] of the as-Synthesized SnO_2, ZnO and SnO_2–ZnO Nanomaterials

photocatalyst	S_{BET} ($m^2\ g^{-1}$)	pore volume ($cm^3\ g^{-1}$)	mean pore size (nm)
SnO_2	90 ± 2.5	0.22 ± 0.005	10 ± 0.5
ZnO	45 ± 1.5	0.29 ± 0.01	26.5 ± 1
SnO_2–ZnO	77 ± 2.0	0.26 ± 0.01	14 ± 0.5

[a]Surface areas were determined by the BET technique, mean pore diameters by BJH theory (applied to the adsorption branch), and pore volumes by single-point analysis.

the pore size distribution for the SnO_2–ZnO photocatalyst was rather large with an average pore diameter of 14 ± 0.5 nm (Figure 4, inset). As a consequence, all these data were consistent with the formation of mesoporous SnO_2–ZnO nanocatalyst.

The optical properties of the various samples prepared were then investigated by UV–Visible diffuse reflectance. The absorption edge for the SnO_2–ZnO photocatalyst was estimated to be about 390 nm, which was shifted toward the visible region compared to that of the pure SnO_2 sample (Figure 5A). The

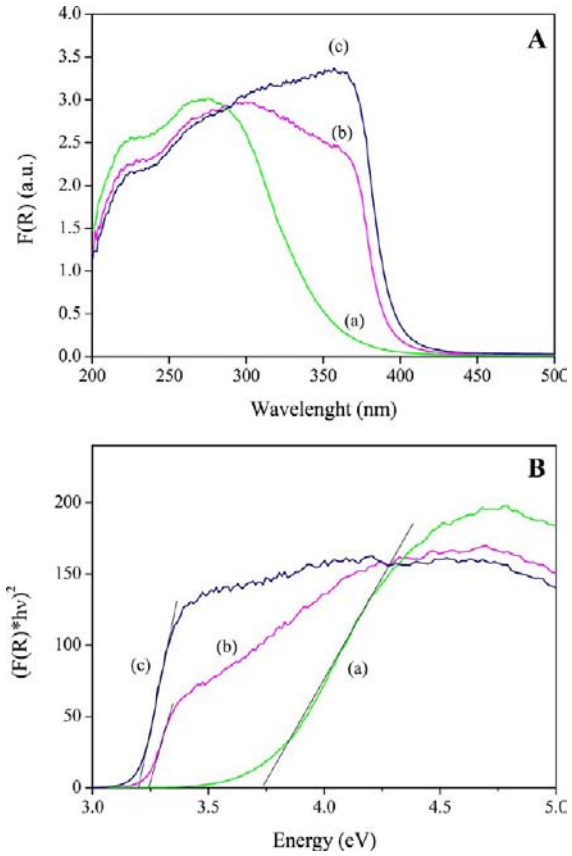

Figure 5. UV–vis diffuse reflectance spectra (**A**) and plots of $(F(R)h\nu)^2$ versus photon energy ($h\nu$) (**B**) of the as-synthesized materials after annealing in air at 500 °C; (a) SnO_2, (b) SnO_2–ZnO, and (c) ZnO.

absorption edges of ZnO and SnO_2 were determined to be 394 and 355 nm, respectively. Compared to the SnO_2 sample, the SnO_2–ZnO photocatalyst showed an obvious absorption edge increment of about 35 nm. The absorption edge at higher wavelengths revealed that the heterostructure photocatalysts could more efficiently utilize light for the photocatalytic purpose.[30] Nonetheless, it was close to that of ZnO because of the 1:1 composition of the heterostructure, since, to some extent, the absorption edge of the heterostructure should be the combined contribution of each component in the SnO_2–ZnO composite.[31] Furthermore, it has been shown for a crystalline direct semiconductor that the optical absorption near the band edge follows the equation $\alpha(h\nu) = A(h\nu - E_g)^{1/2}$ where α, ν, E_g, and A are the absorption coefficient, light frequency, band gap energy, and a constant, respectively.[32] It is generally admitted that the absorption coefficient (α) can be replaced by the remission function, $F(R)$. The latter can be written in terms of diffused reflectance (R) according to the Kubelka–Munk theory: $\alpha/s = F(R) = (1 - R)^2/(2R)$ where s is the scattering coefficient.[33] The band gap energies (E_g values) of the as-synthesized samples can then be estimated from a plot of $(F(R)h\nu)^2 = f(h\nu)$, the intercepts of the tangents yielding the band gap energies of the as-synthesized samples (Figure 5B). The estimated band gap energies of the resulting samples were therefore about 3.7, 3.23, and 3.2 eV for SnO_2, SnO_2–ZnO, and ZnO, respectively. The values for ZnO

dx.doi.org/10.1021/ic300794j | Inorg. Chem. 2012, 51, 7764–7773

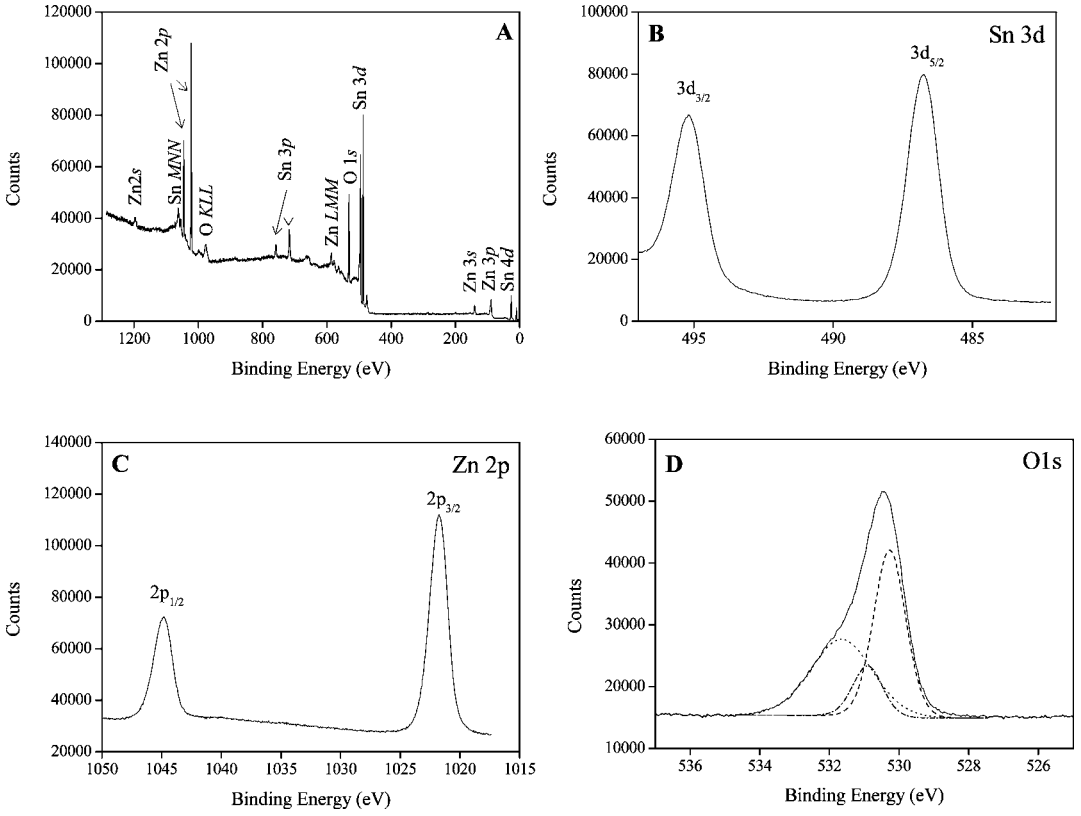

Figure 6. XPS patterns of the SnO_2–ZnO photocatalyst (**A**) XPS survey spectrum; (**B**) Sn 3d region; (**C**) Zn 2p region; (**D**) O1s region (full) with the corresponding fits for OH (dot), O–Zn (dot-dash) and Sn–O–Sn (dash).

and SnO_2 were in good agreement with those reported by others.[34]

3.2. Surface and Interface Analysis. To gain a better insight into the surface composition and the band alignment in the SnO_2–ZnO photocatalyst, XPS studies were performed on the SnO_2, ZnO, and SnO_2–ZnO samples annealed at 500 °C in air. As shown in the survey spectrum of Figure 6A, the SnO_2–ZnO heterostructure only shows emissions of Sn, O, and Zn elements with only a very weak C line, the different peaks observed being assigned to Sn 3d, Sn 3p, Sn 4d, Zn 2p, Zn 3s, and Zn 3p core levels and to Sn *MNN*, Zn *LMM*, and O *KLL* Auger features. The high resolution XPS spectra for Sn 3d (Figure 6B) reveals the spin orbital splitting of the Sn $3d_{5/2}$ and Sn $3d_{3/2}$ core level states of tin centered at 486.8 and 495.2 eV, respectively, which were symmetric and were assigned to the lattice tin oxide. The separation between the Sn $3d_{5/2}$ and Sn $3d_{3/2}$ level (8.41 eV) corresponds to the standard spectrum of Sn[35] and of commercial SnO_2 reported in the literature.[36] The measured emission lines also correspond to a binding energy of Sn^{4+} ion in SnO_2.[35] Figure 6C shows the pronounced splitting of the Zn 2p emission into two symmetric peaks. The peak centered at 1021.8 eV was attributed to the Zn $2p_{3/2}$ and the other one at 1044.9 eV to Zn $2p_{1/2}$, indicating a normal oxidation state of Zn^{2+} in the SnO_2–ZnO photocatalyst. Figure 6D shows the XPS high resolution spectrum of oxygen. The shape of the spectrum is asymmetric which indicates that there are several chemical states according to the measured binding energy. Thus, the region of O 1s could be deconvoluted into three peaks centered at 530.3, 530.8, and 531.5 eV. The lower binding energy peak at 530.3 eV was attributed to oxygen in SnO_2,[37,38] while the peak centered at 530.8 eV is due to the Zn–O binding.[39] The peak at 531.5 eV could be ascribed to adsorbed hydroxyl species.[35,38,40] The results confirmed that the SnO_2–ZnO photocatalyst was actually composed of SnO_2 and ZnO entities. To determine the band alignment of the SnO_2–ZnO nanocatalyst, the core level positions and the VBM positions of bulk SnO_2 and bulk ZnO were also determined.[41] With these values as reference of the energy distance ($E_V - E_{CL}$) for each sample and the energy difference ($E_{CL}^{ZnO} - E_{CL}^{SnO_2}$) the VB line-up can be determined according to eq 1. The VBM positions in the VB spectra were determined by linear extrapolation of the leading edges of the VB spectra of the bulk SnO_2 and ZnO samples to the base lines (Table 2). The energy difference of the Sn $3d_{5/2}$ CL peak to VBM,$(E_{Sn3d} - E_{V\text{-}SnO_2})_{bulk}^{SnO_2}$, was determined to be 483.4 ± 0.05 eV while that of Zn $2p_{3/2}$ to ZnO VBM,$(E_{Zn\text{-}2p} - E_{V,ZnO})_{bulk}^{ZnO}$, was 1019.10 ± 0.05 eV. The energy difference of Sn $3d_{5/2}$ and Zn $2p_{3/2}$ CLs, ΔE_{CL}, in the SnO_2–ZnO heterostructure was evaluated to be 535.0 ± 0.05 eV. According to eq 1, the resulting VB offset (VBO), ΔE_V, was calculated to be 0.7 eV. Finally the CB offset (CBO) was estimated by the formula $\Delta E_C = \Delta E_V + E_g^{ZnO} - E_g^{SnO_2}$, where E_g^{ZnO} and $E_g^{SnO_2}$ are the optical band gap of

Table 2. XPS Binding Energies of the Core Levels and VBM of SnO_2, ZnO, and SnO_2–ZnO Photocatalysts

photocatalyst	state	binding energy (eV)
SnO_2	Sn $3d_{5/2}$	486.70 ± 0.05
	VBM	3.30 ± 0.05
ZnO	Zn $2p_{3/2}$	1021.70 ± 0.05
	VBM	2.60 ± 0.05
SnO_2–ZnO	Sn $3d_{5/2}$	486.80 ± 0.05
	Zn $2p_{3/2}$	1021.80 ± 0.05

dx.doi.org/10.1021/ic300794j | Inorg. Chem. 2012, 51, 7764–7773

ZnO and SnO_2, respectively. Using the band gap of SnO_2 (3.7 eV) and ZnO (3.2 eV) determined by UV−visible diffuse reflectance spectroscopy (Figure 5B), the ΔE_C was calculated to be 0.2 ± 0.05 eV that led to the proposed energy band diagram for the SnO_2−ZnO sample shown in Figure 7. This experimentally determined energy diagram is fully consistent with the formation

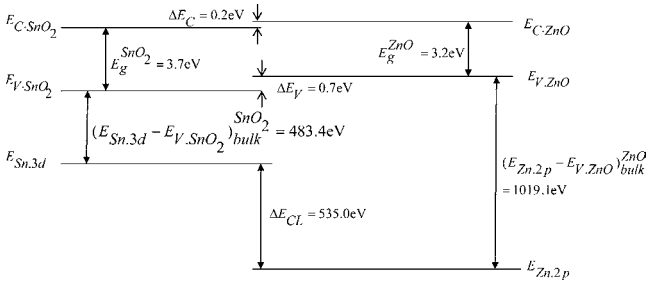

Figure 7. Band alignment diagram of the SnO_2−ZnO photocatalyst.

of mesoporous SnO_2−ZnO type II heterojunction nanomaterials as already schematically drawn in Scheme 1.

3.3. Photocatalytic Activity. To evidence the photocatalytic activities of the as-synthesized SnO_2−ZnO nanomaterials, the photocatalytic decomposition of MB was performed as a test reaction according to the literature.[42] As depicted in Figure 8A, the maximum absorption peaks of MB at 664 nm diminished gradually and disappeared completely under UV light irradiation for 80 min in the presence of the SnO_2−ZnO nanocatalyst. Meanwhile, the color of the solution changed gradually, suggesting that the chromophoric structure of MB was decomposed. Furthermore, blank experiments in the absence of irradiation with the photocatalyst or in the presence of irradiation without the photocatalyst, as well as similar experiments with pure SnO_2 and ZnO samples were carried out to rationalize the photocatalytic activity of the as-synthesized SnO_2−ZnO photocatalyst. The degradation efficiency of the as-synthesized samples was defined as C/C_0, where C_0 is the initial concentration of MB, after equilibrium adsorption, and C its concentration during the reaction. Both blank experiments results showed that MB could not be decomposed without the photocatalyst and/or UV irradiation (Figure 8B). In contrast, the degradation efficiency of the SnO_2−ZnO photocatalyst after 20 min was of about 88%, whereas values of about 72% and 50% were found after 20 min for the SnO_2 and ZnO samples, respectively (Figure 8B). Furthermore, the MB decomposition efficiency found for the SnO_2−ZnO photocatalyst was comparable to that determined under the same experimental conditions for the reference P-25 catalyst, that is, 85% after 20 min. As a result, the heterojunction nanomaterial concept allowed increasing the photocatalytic activities of SnO_2 and ZnO up to that of commercial titania that validates the approach developed in this study. For a better understanding of the photocatalytic efficiency of the as-synthesized samples, the kinetic analysis of MB degradation is discussed in the following. It is generally assumed that reaction kinetics can be described in

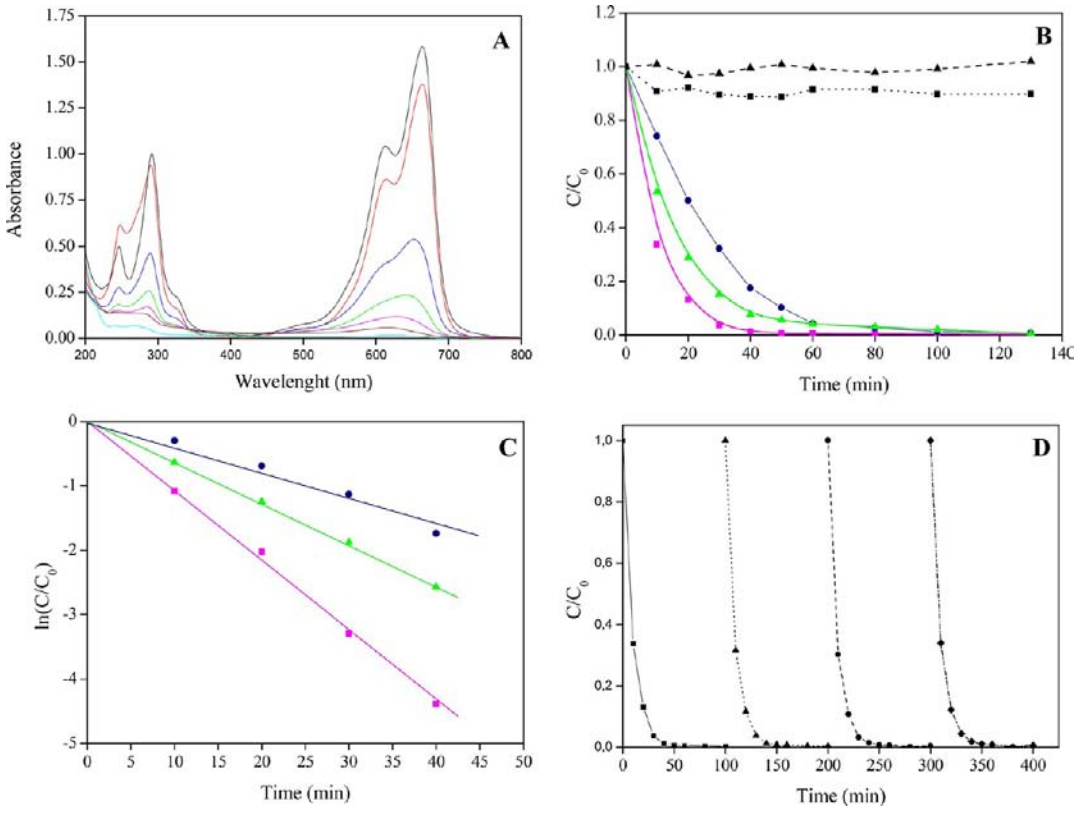

Figure 8. (**A**) Absorbance changes of MB solution after different irradiation times in the presence of the SnO_2−ZnO sample: initial (black), equilibrium (red), 10 min (blue), 20 min (green), 30 min (magenta), 40 min (brown), and 130 min (cyan). (**B**) Kinetic of the degradation of MB in the presence of UV only (square, dot), SnO_2−ZnO in the dark (triangle, dash), SnO_2−ZnO under UV (square, plain), SnO_2 under UV (triangle, plain), and ZnO under UV (circle, plain). (**C**) ln [C/C_0] as a function of the irradiation time for calcined SnO_2 (triangle), SnO_2−ZnO (square), and ZnO (circle) photocatalysts. (**D**) Cyclic runs in the photodegradation of MB using the SnO_2−ZnO photocatalyst under UV-light: 1st cycle (square), 2nd cycle (triangle), 3rd cycle (circle), and 4th cycle (diamond).

dx.doi.org/10.1021/ic300794j | Inorg. Chem. 2012, 51, 7764−7773

terms of Langmuir−Hinshelwood model, which can be expressed following eq 2:[43]

$$-\frac{dC}{dt} = k_r \frac{K_a C}{1 + K_a C} \quad (2)$$

where $(-dC/dt)$ is the degradation rate of MB, C is the concentration of MB, t is the reaction time, k_r is a reaction rate constant, and K_a is the adsorption coefficient of the reactant. As the initial concentration of MB is very low (C_0 = 10 mg/L in the as-described experiments), K_aC is negligible, and eq 2 can be described as first-order kinetics. Setting eq 2 at the initial conditions of the photocatalytic procedure, when $t = 0$, $C = C_0$, it can be described as

$$\ln \frac{C}{C_0} = -k_{app} t \quad (3)$$

where k_{app} is the apparent rate constant, used as the basic kinetic parameter for different photocatalysts, since it enables one to determine a photocatalytic activity independent of the previous adsorption period in the dark, and the concentration of the remaining dye in solution. This model was then applied to the present data (Figure 8C), and the apparent first-order rate constants, before and after normalization by the BET surface area, is reported in Table 3. First of all, the degradation of MB followed a first order kinetic rate for all samples. Furthermore, the

Table 3. Apparent (k_{app}) and Normalized (k_{norm}) Rate Constants for the Degradation of MB with the As-Synthesized Materials[a]

photocatalysts	k_{app} min^{-1}	k_{norm} g/(m^2 min)
SnO_2−ZnO	0.0931	12.1×10^{-4}
SnO_2	0.0635	7.1×10^{-4}
ZnO	0.0401	8.9×10^{-4}

[a] k_{norm} calculated from k_{app} and the BET surface area given in Table 1.

mesoporous SnO_2−ZnO heterojunction nanomaterial was clearly a much more effective photocatalyst than the SnO_2 and ZnO analogues with an apparent MB degradation rate constant reaching 0.0931 min^{-1}. In addition, this nanocatalyst can be recycled and reused several times without significant loss of efficiency, which is a key requirement for a possible industrial application. Thus, the photocatalytic efficiency of the SnO_2−ZnO heterojunction photocatalyst for the 4 cycling reuse were 99.3, 99.2, 99.3, and 99.0% after 50 min of reaction time, respectively (Figure 8D). Finally, it is also worth mentioning that the photocatalytic activity collapsed in acidic solution and was improved in basic medium, the SnO_2−ZnO photocatalyst being always the most efficient.[41] This behavior can be rationalized on the basis of the point of zero charge (pH_{pzc}) of SnO_2 and ZnO that is about 4 and 9, respectively. Indeed, since MB is a cationic dye, the dye chemisorption at the oxide surface will be favored by negatively charged metal oxide nanoparticles, that is, in basic medium.

In summary, the improved photocatalytic activity found for the SnO_2−ZnO heterostructure can be rationalized on the basis of the above-determined band alignment as follows (Scheme 1 and 2). Upon UV illumination, electrons in the VB could be excited to the CB of both oxides, with the concomitant formation of the same amount of holes in the VB. According to the type II band alignment and the heterojunction formed, the electrons were collected by the SnO_2 nanosized particles and the holes by the

Scheme 2. Proposed Mechanism for the Degradation of MB under UV Irradiation in the Presence of the SnO_2−ZnO Photocatalyst

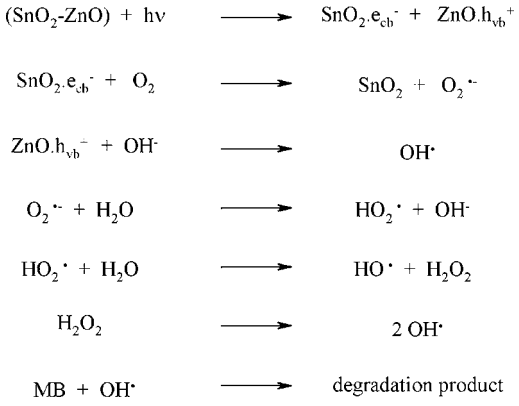

ZnO particles as they are transferred to a more stable electronic state, that is, downward for electron transfer from ZnO to SnO_2, upward corresponding to a more stable bonding situation for holes from SnO_2 to ZnO (Comparison between Scheme 1 left, and Figure 7.). The resulting charge carrier separation (electrons preferentially on the SnO_2 particle, holes preferentially at the ZnO particle) leads to increased carrier lifetime because of reduced charge recombination. As a consequence, the formation of hydroxyl OH$^\bullet$ radicals by reaction of holes with surface hydroxyl groups or physisorbed water molecules at the zinc oxide surface is enhanced. On the other side, also the reaction of electrons with dissolved oxygen molecules to give superoxide radical anions, $O_2^{\bullet -}$, yielding hydroperoxyl radicals $HO_2^\bullet$ on protonation and finally OH$^\bullet$ radicals will be more efficient. OH$^\bullet$ radicals are a strong oxidizing agent well-known to decompose organic substrates as MB dye.[44] As a result, the enhanced charge separation related to the SnO_2−ZnO heterojunction favors the interfacial charge transfer to physisorbed species forming OH$^\bullet$ radicals and reduce possible back reactions, and therefore accounts for the higher activity of the SnO_2−ZnO nanomaterials.

4. CONCLUSION

Mesoporous SnO_2−ZnO heterojunction photocatalysts have been successfully prepared using a two-step solution route involving the synthesis of nanosized SnO_2 particles by the homogeneous precipitation combined with a hydrothermal treatment that were further reacted with zinc acetate followed by calcination. The UV−vis diffuse reflectance studies showed that the band gap energy of the heterostructure SnO_2−ZnO photocatalyst was red-shifted compared to that of pure SnO_2 and ZnO. A careful examination of the band alignment by XPS revealed a type-II band alignment with VBO of $\Delta E_V = 0.7 \pm 0.05$ eV and CBO of $\Delta E_C = 0.2 \pm 0.05$ eV for the SnO_2−ZnO heterojunction photocatalyst. This heterojunction photocatalyst showed higher photocatalytic activity than the pure SnO_2 and ZnO nanocatalysts for the degradation of MB dye under UV light irradiation in neutral and basic media because of improved separation of photogenerated electrons and holes. Furthermore, the heterostructure photocatalysts could be easily recycled without significant change in the catalytic activity which evidenced the stability of the catalysts and the reproducibility of the approach. This concept of semiconducting heterojunction nanocatalysts with high photocatalytic activity should find industrial application in the future to remove undesirable organics from the environment.

dx.doi.org/10.1021/ic300794j | Inorg. Chem. 2012, 51, 7764−7773

■ ASSOCIATED CONTENT

Supporting Information

Additional information and figures concerning XPS and photocatalytic studies (reference experiment with P25). This material is available free of charge via the Internet at http://pubs.acs.org.

■ AUTHOR INFORMATION

Corresponding Author

*E-mail: t.toupance@ism.u-bordeaux1.fr.

Notes

The authors declare no competing financial interest.

■ ACKNOWLEDGMENTS

Dr. Jörg Zimmermann (TUD) and Mrs. Odile Babot (ISM) are thanked for the UV−vis diffused reflectance spectrometry and N_2 sorption measurements, respectively. This work was carried out within the framework of EMMI (European Multifunctional Material Institute) and was supported by the Erasmus Mundus Joint Doctoral program International Doctoral School in Functional Materials for Energy, Information Technology and Health (T.U. fellowship), and the Aquitaine Region (Contract no.11002746).

■ REFERENCES

(1) (a) Hoffmann, M. R.; Martin, S. T.; Choi, W.; Bahnemann, D. W. *Chem. Rev.* **1995**, *95*, 69. (b) Tennakone, C. T.; Tilakarante, C. T. K.; Kottegoda, I. R. M. *J. Photochem. Photobiol. A: Chem.* **1995**, *87*, 177. (c) Habibi, M. H.; Vosooghian, H. *J. Photochem. Photobiol. A: Chem.* **2005**, *174*, 45. (d) Liu, C. C.; Hsieh, Y. H.; Lai, P. F.; Li, C. H.; Kao, C. L. *Dyes Pigm.* **2006**, *68*, 191.

(2) (a) Linsebigler, A. L.; Lu, G.; Yates, J. T. *Chem. Rev.* **1995**, *95*, 735. (b) Mahmoodi, N. M.; Arami, M.; Limaee, N. Y.; Tabrizi, N. S. *J. Colloid Interface Sci.* **2006**, *295*, 159. (c) Rauf, M. A.; Ashraf, S. S. *Chem. Eng. J.* **2009**, *151*, 10. (d) Behnajady, M. A.; Modirshahla, N.; Daneshvar, N.; Rabbani, M. *J. Hazard. Mater.* **2007**, *140*, 257.

(3) Zhang, M.; Sheng, G.; Fu, J.; An, T.; Wang, X.; Hu, X. *Mater. Lett.* **2005**, *59*, 3641.

(4) Bedja, I.; Kamat, P. V. *J. Phys. Chem.* **1995**, *99*, 9182.

(5) (a) Jiang, Y.; Sun, Y.; Liu, H.; Zhu, F.; Yin, H. *Dyes Pigm.* **2008**, *78*, 77. (b) Liao, D. L.; Badour, C. A.; Liao, B. Q. *Photochem. Photobiol. A: Chem.* **2008**, *194*, 11. (c) Tian, J.; Chen, L.; Yin, Y.; Wang, X.; Dai, J.; Zhu, Z.; Liu, X.; Wu, P. *Surf. Coat. Technol.* **2009**, *204*, 205. (d) Darzi, S. J.; Mahjoub, A. R. *J. Alloys Compd.* **2009**, *486*, 805. (e) Zhang, M.; An, T.; Liu, X.; Hu, X.; Sheng, G.; Fu, J. *Mater. Lett.* **2010**, *64*, 1883. (f) Liu, R.; Ye, H.; Xiong, X.; Liu, H. *Mater. Chem. Phys.* **2010**, *121*, 432.

(6) (a) Shifu, C.; Lei, C.; Shen, G.; Gengyu, C. *Powder Technol.* **2005**, *160*, 198. (b) Leghari, S. A. K.; Sajjad, S.; Chen, J.; Zhang, J. *Chem. Eng. J.* **2011**, *166*, 906. (c) Lv, K.; Li, J.; Qing, X.; Li, W.; Chen, Q. *J. Hazard. Mater.* **2011**, *189*, 329. (d) Ismail, M.; Bousselmi, L.; Zahraa, O. *Photochem. Photobiol. A: Chem.* **2011**, *222*, 314.

(7) (a) Li, D.; Haneda, H. *J. Photochem. Photobiol. A: Chem.* **2003**, *160*, 203. (b) Yu., C.; Yang, K.; Shu, Q.; Yu, J. C.; Cao, F.; Li, X. *Chin. J. Catal.* **2011**, *32*, 555.

(8) (a) Wang, Y.; Lee, J. Y.; Zeng, H. C. *Chem. Mater.* **2005**, *17*, 3899. (b) Lou, X. W.; Wang, Y.; Yuan, C.; Lee, J. Y.; Archer, L. A. *Adv. Mater.* **2006**, *17*, 2325. (c) Ha, H.-W.; Kim, K.; de Borniol, M.; Toupance, T. *J. Solid State Chem.* **2006**, *179*, 689.

(9) He, H., Jr; Wu, T. H.; Hsin, C. L.; Li, K. M.; Chen, L. J.; Chueh, Y. L.; Chou, L. J.; Wang, Z. L. *Small* **2006**, *2*, 116.

(10) (a) Gurlo, A. *ChemPhysChem* **2006**, *7*, 241. (b) Gurlo, A.; Riedel, R. *Angew. Chem., Int. Ed.* **2007**, *46*, 3826. (c) Nayral, C.; Viala, E.; Fau, P.; Senocq, F.; Jumas, J.-C.; Maisonnat, A.; Chaudret, B. *Chem.—Eur. J.* **2000**, *6*, 4082. (d) Han, C. H.; Han, S.-D.; Singh, I.; Toupance, T. *Sens. Actuators, B* **2005**, *109*, 264. (e) Pavelko, R. G.; Daly, H.; Hardacre, C.; Vasiliev, A. A.; Llobet, E. *Phys. Chem. Chem. Phys.* **2010**, *12*, 2639. (f) Marichy, C.; Donato, N.; Willinger, M.-G.; Latino, M.; Karpinsky, D.; Yu, S. H.; Neri, G.; Pinna, N. *Adv. Mater.* **2011**, *21*, 658.

(11) (a) Vilaça, G.; Jousseaume, B.; Mahieux, C.; Belin, C.; Cachet, H.; Bernard, M.-C.; Vivier, V.; Toupance, T. *Adv. Mater.* **2006**, *18*, 1073. (b) Gubbala, S.; Chakrapani, V.; Kumar, V.; Sunkara, M. K. *Adv. Funct. Mater.* **2008**, *18*, 2411. (c) Liu, J.; Luo, T.; Mouli, S.; Meng, F.; Sun, B.; Li, M.; Liu, J. *Chem. Commun.* **2010**, *46*, 472. (d) Tebby, Z.; Uddin, T.; Olivier, C.; Nicolas, Y.; Toupance, T.; Hirsch, L. *ACS Appl. Mater. Interfaces* **2011**, *3*, 1485.

(12) (a) Cun, W.; Jincai, Z.; Xinming, W.; Bixian, M.; Guoying, S.; Ping'an, P.; Jiamo, F. *Appl. Catal., B* **2002**, *39*, 269. (b) Cun, W.; Wang, X.; Xu, B.; Zhao, J.; Mai, B.; Ping'an, P.; Sheng, G.; Jiamo, F. *J. Photochem. Photobiol. A: Chem.* **2004**, *168*, 47. (c) Zhang, M.; An, T.; Hu, X.; Wang, C.; Sheng, G.; Fu, J. *Appl. Catal., A* **2004**, *260*, 215. (d) Zhang, M.; Sheng, G.; Fu, J.; An, T.; Wang, X.; Hu, X. *Mater. Lett.* **2005**, *59*, 3641. (e) Wang, H.; Baek, S.; Lee, J.; Lim, S. *Chem. Eng. J.* **2009**, *146*, 355. (f) Yang, Z.; Lv, L.; Dai, Y.; Xv, Z.; Qian, D. *Appl. Surf. Sci.* **2010**, *256*, 2898.

(13) (a) Wen, Z.; Wang, G.; Lu, W.; Wang, Q.; Zhang, Q.; Li, J. *Cryst. Growth Des.* **2007**, *7*, 172. (b) Wang, W.-W.; Zhu, Y.-J.; Yang, L.-X. *Adv. Funct. Mater.* **2007**, *17*, 59. (c) Zheng, L.; Zheng, Y.; Chen, C.; Zhan, Y.; Lin, X.; Zheng, Q.; Wei, K.; Zhu, J. *Inorg. Chem.* **2009**, *48*, 1819.

(14) Zhang, Z.; Shao, C.; Li, X.; Zhang, L.; Xue, H.; Wang, C.; Liu, Y. *J. Phys. Chem. C* **2010**, *114*, 7920.

(15) Baik, N. S.; Sakai, G.; Miura, N.; Yamazoe, N. *Sens. Actuators B* **2000**, *63*, 74.

(16) Parida, K. M.; Dash, S. S.; Das, D. P. *J. Colloid Interface Sci.* **2006**, *298*, 787.

(17) Barrett, E. P.; Joyner, L.; Halenda, P. P. *J. Am. Chem. Soc.* **1951**, *73*, 373.

(18) (a) Lang, O.; Klein, A.; Pettenkofer, C.; Jaegermann, W.; Chevy, A. *J. Appl. Phys.* **1996**, *80*, 3817. (b) Schlaf, R.; Lang, O.; Pettenkofer, C.; Jaegermann, W. *J. Appl. Phys.* **1999**, *85*, 2732. (c) Mönch, W. In *Semiconductor surfaces and interfaces*; Springer-Verlag: Heidelberg, Germany, 1993.

(19) Bernède, J. C.; Barreau, N.; Marsillac, S.; Assmann, L. *Appl. Surf. Sci.* **2002**, *195*, 222.

(20) Song, K. C.; Kang, Y. *Mater. Lett.* **2000**, *42*, 283.

(21) Sibu, C. P.; Kumar, S. R.; Mukundan, P.; Warrier, K. G. K. *Chem. Mater.* **2002**, *14*, 2876.

(22) Chen, D.; Gao, L. *J. Colloid Interface Sci.* **2004**, *279*, 137.

(23) Ismail, H. M. *J. Anal. Appl. Pyrolysis* **1991**, *21*, 315.

(24) (a) Damen, T. C.; Porto, S. P. S.; Tell, B. *Phys. Lett.* **1966**, *144*, 570. (b) Khan, A.; Kordesch, M. E. *Mater. Lett.* **2008**, *62*, 230.

(25) (a) Scott, J. F. J. *Chem. Phys.* **1970**, *53*, 852. (b) Kumar, V.; Govind, A.; Nagarajan, R. *Inorg. Chem.* **2011**, *50*, 5637.

(26) Xu, C. X.; Sun, X. W.; Zhang, X. H.; Ke, L.; Chua, S. J. *Nanotechnology* **2004**, *15*, 856.

(27) Loridant, S. *J. Phys. Chem. B* **2002**, *106*, 13273.

(28) Sing, K. S. W.; Everett, D. H.; Haul, R. A. W.; Moscou, L.; Pierotti, R. A.; Rouquerol, J.; Siemieniewska, T. *Pure Appl. Chem.* **1985**, *57*, 603.

(29) (a) Leofanti, G.; Padovan, M.; Tozzola, G.; Venturelli, B. *Catal. Today* **1998**, *41*, 207. (b) Toupance, T.; El Hamzaoui, H.; Jousseaume, B.; Riague, H.; Saadeddin, I.; Campet, G.; Broetz, J. *Chem. Mater.* **2006**, *18*, 6364.

(30) Shifu, C.; Lei, C.; Shen, G.; Gengyu, C. *Powder Technol.* **2005**, *160*, 198.

(31) Liu, R.; Ye, H.; Xiong, X.; Liu, H. *Mater. Chem. Phys.* **2010**, *121*, 432.

(32) Davis, E. A.; Mott, N. F. *Phil. Mag.* **1970**, *22*, 903.

(33) Jahan, F.; Islan, M. H.; Smith, B. E. *Sol. Energy Mater. Sol. Cells* **1995**, *37*, 383.

(34) (a) Hagfelt, A.; Gratzel, M. *Chem. Rev.* **1995**, *95*, 49. (b) Lin, C. F.; Wu, C. H.; Onn, Z. N. *J. Hazard. Mater.* **2008**, *154*, 1033. (c) Memming, R. *Electrochim. Acta* **1980**, *25*, 77. (d) Vogel, R.; Hoyer, P.; Weller, H. *J. Phys. Chem.* **1994**, *98*, 3183.

(35) Moulder, J. F.; Sticke, W. F.; Sobol, K. P. E.; Bomben, D. In *Handbook of X-ray photoelectron spectroscopy*; Chastain, J., King, R. C., Jr.,

Eds.; Physical Electronics Division, Perkin-Elmer Corp: Eden Prairie, MN, 1995; p 127.
(36) Babar, A. R.; Shinde, S. S.; Moholkar, A. V.; Rajpure, K. Y. *J. Alloys Compd.* **2010**, *505*, 743.
(37) Chang, S. T.; Leu, I. C.; Hon, M. H. *J. Cryst. Growth* **2004**, *273*, 195.
(38) Li, G.; Leung, M. K. H. *J. Sol-Gel Sci. Technol.* **2010**, *53*, 499.
(39) Ballerini, G.; Ogle, K.; Labrousse, M. G. B. *Appl. Surf. Sci.* **2007**, *253*, 6860.
(40) Mu, J.; Shao, C.; Guo, Z.; Zhang, Z.; Zhang, M.; Zhang, P.; Chen, B.; Liu, Y. *ACS Appl. Mater. Interfaces* **2011**, *3*, 590.
(41) See Supporting Information.
(42) (a) Guo, Y.; Wang, H.; He, C.; Qiu, L.; Cao, X. *Langmuir* **2009**, *25*, 4678. (b) Logar, M.; Jancar, B.; Sturm, S.; Suvorov, D. *Langmuir* **2010**, *26*, 12215. (c) Hirose, Y.; Mori, T.; Morishita, Y.; Itadani, A.; Kudoh, T.; Ohkubo, T.; Matsuda, T.; Kittaka, S.; Kuroda, Y. *Inorg. Chem.* **2011**, *50*, 9948. (d) Kang, J.; Kuang, Q.; Xie, Z.-X.; Zheng, L.-S. *J. Phys; Chem. C* **2011**, *115*, 7874.
(43) Burch, R.; Breen, J. P.; Meunier, F. C. *Appl. Catal., B* **2002**, *39*, 283.
(44) (a) Tayade, R. J.; Sivakumar, T. S.; Bajaj, H. C. *Ind. Eng. Chem. Res.* **2009**, *48*, 10262. (b) Zhang, L.; Yin, L.; Wang, C.; Lun, N.; Qi, Y. *ACS Appl. Mater. Interfaces* **2010**, *2*, 1769.